applied sciences

MDPI

Article

The Effect of Bayer Red Mud Blending on the Mechanical Properties of Alkali-Activated Slag-Red Mud and the Mechanism

Juntong Li [1], Qing Li [1,2,3,*], Ping Chen [1,2], Kai Yao [1], Penghuai Wang [1], Yang Ming [2,3], Jin Yi [2] and Lili Zhi [2]

[1] College of Materials Science and Engineering, Guilin University of Technology, Guilin 541004, China
[2] Guangxi Engineering and Technology Center for Utilization of Industrial Waste Residue in Building Materials, Guilin 541004, China
[3] Collaborative Innovation Center for Exploration of Nonferrous Metal Deposits and Efficient Utilization of Resources in Guangxi, Guilin 541004, China
* Correspondence: liqing@glut.edu.cn; Tel.: +86-139-8365-1341

Abstract: In this paper, Bayer red mud and ground granulated blast furnace slag were formed into three different ratios (7:3, 5:5 and 3:7) of alkali-activated cementitious materials (AASR) using a water glass solution as the alkali activator. By studying the compressive strength of different red mud content, the effect of Bayer red mud content on the mechanical properties of AASR was analyzed. The influence mechanism of red mud content on the mechanical properties of AASR was revealed by the variation of micro-porosity, connected porosity, Isothermal calorimetry, XRD, FTIR, and BSE/EDS testing techniques. The results show that the compressive strength of the specimens at the same age decreases with the increase of red mud content. On one hand, the addition of red mud makes the connected porosity in the AASR system increase, and the densification of the slurry structure decreases; on the other hand, the inert minerals in red mud participate in the hydration reaction to a lesser extent, the overall hydration reaction process becomes lower, and the generation of hydration products providing strength decreases.

Keywords: Bayer red mud; alkali-activated materials; compressive strength; pore structure; BSE/EDS

check for updates

Citation: Li, J.; Li, Q.; Chen, P.; Yao, K.; Wang, P.; Ming, Y.; Yi, J.; Zhi, L. The Effect of Bayer Red Mud Blending on the Mechanical Properties of Alkali-Activated Slag-Red Mud and the Mechanism. *Appl. Sci.* **2023**, *13*, 452. https://doi.org/10.3390/app13010452

Received: 7 December 2022
Revised: 22 December 2022
Accepted: 27 December 2022
Published: 29 December 2022

Copyright: © 2022 by the authors. Licensee MDPI, Basel, Switzerland. This article is an open access article distributed under the terms and conditions of the Creative Commons Attribution (CC BY) license (https://creativecommons.org/licenses/by/4.0/).

1. Introduction

Bayer red mud is the residue of alumina produced by the Bayer process, after the dissolution of bauxite with caustic soda, which is characterized by a high water content, a small particle size, and a high alkali content with an average pH value of 11.3 ± 1.0 [1,2]. This is also a toxic industrial waste, with a global stockpile of over 2.7 billion tons, causing great harm to the environment [3]. With the intensification of environmental and lack of resources problems, the environmentally sound and comprehensive utilization of red mud has become an important research topic with regard to sustainability.

Using Bayer red mud, ground granulated blast furnace slag and a certain ratio of alkali activator to prepare a new clinker-free water-hardenable cementitious material, namely, alkali- activated slag-red mud (AASR) is a promising approach which can offer high strength development, high resistance against chloride ingress, high resistance against chemical attacks, and superior durability [4,5]. The development of AASR and its related technologies cannot only make full use of the residual value of red mud to reduce the consumption of natural resources, but can also solve the environmental problems caused by red mud stockpiling. In addition, the use of AASR to replace ordinary silicate cement (OPC) can reduce CO_2 emissions by more than 75% and energy consumption by 60% [6]. Therefore, AASR has a rather broad application prospect, and is thus favored by scholars at home and abroad.

The basic mechanical properties are a vital fundamental parameter and an important prerequisite for the application of AASR, so as to judge, understand and optimise the

performance of AASR; however, the research on the mechanical properties of AASR is still in its initial stages. It is also important to mention that there are differences in the research results of scholars from different institutions and regions [4,7,8]. Chen et al. prepared alkali-activated slag-red mud material with a 30% red mud admixture using Na_2SiO_3 of 6.9% alkali equivalent (modulus 1.7) after drying and activating the red mud at 100 °C, having found that the compressive strength at 24 h of curing was 18.53 Mpa [9]. Lemougna et al. finely ground the dried red mud and used Na_2SiO_3 at 30% concentration (modulus 2.0) to prepare alkali-activated slag-red mud material with 50% red mud admixture, having found a compressive strength of 86 MPa after 28 days [10]. Zhang Peng et al. activated red mud at high temperature, and prepared an AASR with a 60% red mud admixture using Na_2SiO_3-3.2H_2O (modulus 2.4), having found a compressive strength of 76 MPa after 48 h of curing [11]. Garanayak et al. found that 50% of red mud and 50% of slag obtained the highest strength, with an alkali exciter of modulus 1.5, and that calcium vanadinite and C-S-H gels were responsible for the development of the strength of alkali excited slag red mud cementitious material [12]. Liang pointed out that when the calcination temperature of red mud is 700 °C, the Si-O bonds and Al-O bonds break, thus showing good mechanical properties [13]. Gao et al. prepared and found feasible belite-rich sulphoaluminate cement repair material based on synergistic theory using red mud, slag and desulfurization gypsum [14]. Kaige Tian verified the appropriate amounts of RM that enabled the promoting of the alkali-activated reaction of slag [15]. Clearly, the mechanical properties of AASR are affected by several factors, such as the dosage of red mud, the type and dosage of the alkali activator, the modulus of the water glass, the maintenance method of red mud, and the treatment method of red mud, etc., among which the dosage of red mud is one of the most basic influencing factors. Although previous studies suggest that the mineral composition of Si, Al, Na and their oxides are the main factors that affect the strength of AASR, many differences in the experimental results cannot be explained from the perspective of chemical mineral composition alone, and there is an urgent need to further investigate the effect of red mud with the addition of the basic mechanical properties of AASR, as well as to dissect the internal reaction mechanism.

The purpose of this article is to investigate the effect of red mud by adding the mechanical properties of AASR, and to clarify its mechanism by heat of hydration, X-ray powder diffraction (XRD), Fourier-transform infrared spectroscopy (FTIR), pore structure, and backscattered electrons (BSE)/energy dispersive X-ray spectroscopy (EDS) tests.

2. Materials and Methods

2.1. Source Materials

Ground granulated blast furnace slag (GGBFS) was supplied by the Guangxi Guigang Iron and Steel Company. The specific surface area of the slag was determined to be 394 m^2/kg, and the density was 2.91 g/cm^3 according to Burr's specific surface area method, after which the slag was ball-milled and sieved. The Bayer red mud used in this study was from Guangxi Province, China. The material was dried at 105 °C for 24 h and sieved. The specific surface area was determined to be 670 m^2/kg and its density was 3.11 g/cm^3.

A water glass was used as an activator, and its modulus (SiO_2/Na_2O molar ratio) was 1.8 in this study. It was prepared by mixing a solution of NaOH and commercial sodium silicate (modulus: 3.34) in the pre-calculated ratio. AASRs were prepared using a water glass with a (Na_2O) concentration of 5 wt.% of cementitious components. Before mixing with the AASR mixture, the alkaline solution was cooled at 20 (±1) °C for 2 h to avoid the potential effect of the solution's heat on the experimental results.

The main chemical compositions of the red mud and blast furnace slag was determined by X-ray fluorescence spectroscopy (XRF), which was done a ZSX Primus, and the results are shown in Table 1. The particle size distribution (PSD) of red mud and slag were tested by using a Morphology 4 laser diffraction analyzer, as shown in Figure 1. Those were

expressed as volume percentage and cumulative volume percentage. On comparison of the base materials, RM was found to be finer than GGBFS.

Table 1. Chemical compositions of slag and red mud (wt. %).

Binder	SiO_2	Al_2O_3	Fe_2O_3	MgO	CaO	Na_2O	K_2O	SO_3	TiO_2
Slag	30.79	13.56	0.96	8.18	41.59	0.40	0.46	2.12	0.94
Red Mud	13.49	20.39	30.58	0.32	15.82	9.15	0.19	0.66	7.80

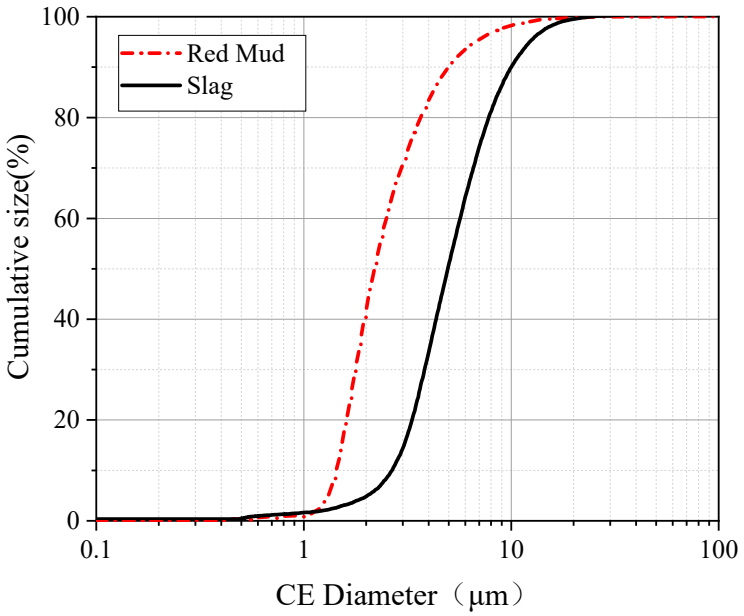


Figure 1. Particle size distribution of RM and GGBFS.

The XRD spectra of both GGBFS and RM are shown in Figure 2. It is clear that GGBFS is primarily composed of a glass phase, while the main phase compositions of RM are Hematite (Fe_2O_3), Katoite ($Ca_3Al_2SiO_4(OH)_8$), Diaspore (AlO(OH), Calcite ($CaCO_3$) and Cancrinite ($Al_6C_{1.44}H_{4.88}Na_8O_{30.32}Si_6$).

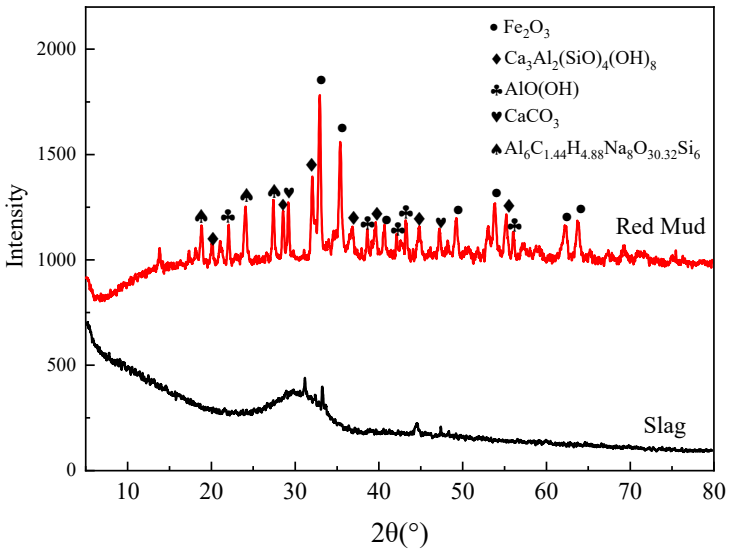


Figure 2. XRD patterns of RM and GGBFS.

2.2. Experimental Programme

2.2.1. Specimens Preparation and Test Procedure

Table 2 gives the mix proportions of AASR that were used in this study. The GGBFS and RM were first mixed in a mixing pot at low speed for 30 s and then mixed with the pre-prepared water glass, stirred at high speed for 30 s, and stopped for 30 s in between, during which the edge paste was scraped into the mixing pot. After mixing, specimens were vibrated on a shaking table until no air bubbles appeared on the surface, and they were then covered with a polyethylene film to prevent water loss. The samples were then unmoulded after 24 h and cured in a standard room (20 (±2) °C, relative humidity > 95%) until the test.

Table 2. AASR pastes mixture proportions (per group).

Binder	GGBFS/g	RM/g	WG/g	NaOH/g	Water/g
AAS-Control	500	/	157.15	15.39	136.16
AAS-30%RM	350	150	157.15	15.39	136.16
AAS-50%RM	250	250	157.15	15.39	136.16
AAS-70%RM	150	350	157.15	15.39	136.16

2.2.2. Test Procedures

(1) Compressive strength: The compressive strength of AASR samples were determined at the age of 3, 7, 14 and 28 days according to the Chinese National Standard GB/T17671-1999 [16]. All of the results of compressive strength reported the average value of three samples.

(2) Porosity: The connected porosity was assessed by measuring accessible porosity according to ASTMC642 [17]. The paste specimens of the specified age were immersed in a water tank at 20 °C for 72 h. The moisture was then removed from the surface with a towel, and the mass of the surface-dried specimen was determined (m_{imm}, g); The samples were then suspended by a wire to determine their apparent mass in water (m_{sus}, g), and after this, the samples were dried in an oven at a temperature of 40 (±5) °C to a constant weight, and the mass was recorded as $m_{40^{\circ}\mathrm{C\text{-}dry}}$ (g). The connected porosity was calculated according to the following equation:

$$\phi_C = \frac{\left(m_{\mathrm{imm}} - m_{40^{\circ}\mathrm{C-dry}}\right)}{\rho_{\mathrm{w}} V}$$

where ϕ_C is the sample connected porosity (%); m_{imm} is the mass of saturated sample (g); $m_{40^{\circ}\mathrm{C-dry}}$ is the constant mass of sample dried at 40 °C (g); ρ_{w} is the density of water (g/cm^3); and V is the bulk volume of cement paste (cm^3).

Micro-porosity: In addition to the connected porosity, the AASR specimens also contain micro-pores (most of which are gel pores), which reflect the changes in the microstructure properties of specimens. In this study, referring to the existing studies [18–20], the mass loss of the samples dried between 40 °C and 105 °C are used to determine the micro-porosity via the following equation:

$$\phi_M = \frac{\left(m_{40^{\circ}\mathrm{C-}dry} - m_{105^{\circ}\mathrm{C-dry}}\right)}{\rho_{\mathrm{w}} V}$$

where ϕ_M is the paste micro-porosity (%); $m_{40^{\circ}\mathrm{C-dry}}$ is the constant mass of samples dried at 40 °C (g); $m_{105^{\circ}\mathrm{C-dry}}$ is the constant mass of samples dried at 105 °C (g); ρ_{w} is the density of water (g/cm^3); and V is the bulk volume of cement paste (cm^3).

(3) Isothermal calorimetry: The hydration process of all the pastes was monitored by hydration heat analysis with an isothermal calorimeter (TAM Air Thermometric, I-CAL4000/8000 Made by Calmetrix Corporation, Boston, MA, USA set at 25 °C). In order to

ensure a precise binder content and a temperature close to the measurement temperature when the sample was charged, all raw materials were stored in the calorimeter at 25 °C for 24 h prior to mixing, and 30.00 g paste was prepared directly in the calorimeter sample cup. Manual mixing with a disposable spoon was applied for the desirable homogeneity, and the hand mixing lasted for 90 s. In order to minimize any loss of binder, the spoon was left in the sample cup after mixing. Measurements were taken every minute for 168 h.

(4) XRD analyses: The 28-day paste samples were crushed and ground into powders followed by drying in a vacuum oven at 40 °C, and then the powders are sieved through a 200-mesh sieve. After this, the powders were sandwiched flat between low absorbing films of a PANalytical's XPert Pro X-ray diffractometer with a configuration of convergent beam with a focalizing mirror. Ni-filtered Cu (Ka) was produced by an X-ray tube operating at 40 kV voltage and 40 mA current. Crystalline phases of the samples were identified at the scanned range of 5°–80° with a dwell time of 0.5 s and a scanning speed of 0.02°/min.

(5) FTIR analyses: A 5DXC Fourier transform infrared spectrophotometer from Nicolet, MA, USA was used in absorption mode to acquire an infrared spectrum which reflects the chemical groups in the reaction products of 28-day samples. The FTIR spectra in the wavenumber range from 4000 to 400 cm^{-1} and were obtained at the spectral resolution of 2 cm^{-1} using the KBr pellet method (i.e., 1 mg dried powder sample per 100 mg KBr), and each spectrum is an average of 32 scans.

(6) BSE/EDS: Specimens were cut about 5 mm with a precision cutter, and dried under a vacuum at 40 °C for 24 h at the testing age. The specimens were then vacuum dried for 24 h at a temperature of 40 (±2) °C, after which specimens were fully filled in a container with low-viscosity epoxy resin. The samples were then coated with gold after being polished with a polishing machine to flatten them to 1 mm. The ULTIM MAX equipped with a tungsten filament emission source was used to capture the images of samples with a back scattered electron detector. The elements in the reaction products were determined by an energy dispersive spectroscopy detector in surface scanning mode.

3. Results and Discussion

3.1. Compressive Strength and Setting Time of AASR

The compressive strength of each specimen is shown in Figure 3. Overall, the compressive strength of AASR increases with age for all mixes, and their strength for a given age decreases with the increase of RM. Interestingly, as 30% RM was added, the compressive strength of specimens developed faster than that of the control mix (especially in the first 7 days), and the 28-day compressive strength reaches to about 77.5 MPa. However, when the amount of RM was increased to 50%, the increase rate of compressive strength became lower, and the 28-day compressive strength decreased to about 57.5 MPa; and when the amount of RM admixture increased to 70%, the development of the compressive strength of the specimens slowed down further, and the compressive strength decreased at all ages significantly, as only 20.2 MPa was obtained after 28 days. This could mainly be attributed to the following two aspects: the introduction of an appropriate amount of RM keeps AASR system at a higher alkalinity, which is helpful to the development of compressive strength, and the excessive amount of RM with low-activity results in less hydration products being formed in AASR due to the dilution effect, which leads to a poor development of compressive strength.

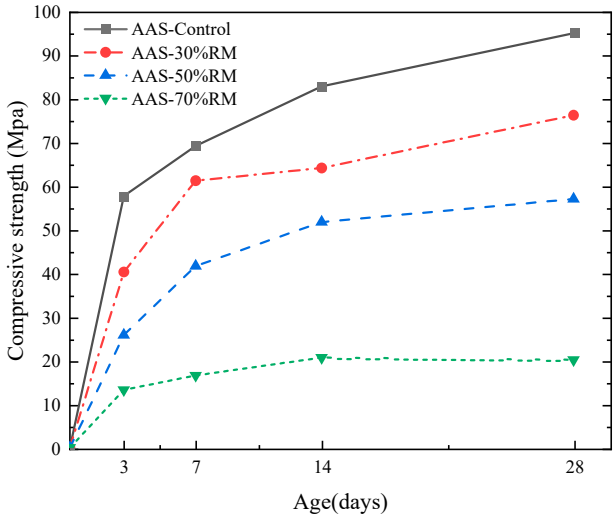


Figure 3. Compressive strength of AASR.

The initial and final setting times of AASR with different RM content is shown in Figure 4. From Figure 4, it can be seen that the setting time of AASR is prolonged with the increase of red mud admixture, which is mainly because the dissociation of red mud is more difficult and slows down the hydration process of the whole system, (which can be confirmed from Section 3.2), so the setting times are prolonged.

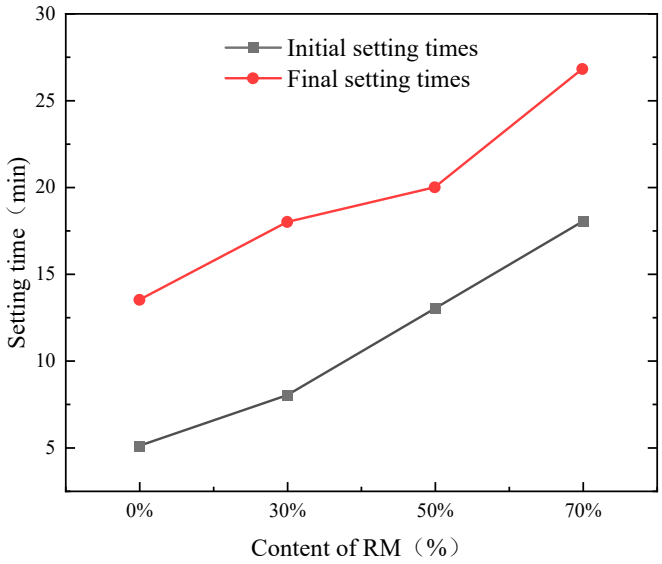


Figure 4. Effect of different red mud additions on the setting time of AASR.

To further explore the mechanisms behind these findings, the porosity, reaction process, reaction products and micro structure were carefully examined, and the results are presented in the following sections.

3.2. The Mechanism of Bayer Red Mud Admixture on the Compressive Strength of AASR

3.2.1. Porosity

The connected porosity and micro-porosity of the control specimens and AASRs are shown in Figure 5. From Figure 5a, it can be seen that the connected porosity of the control group becomes smaller as the age increases, which occurs because the cementitious material continues to hydrate and makes the microstructure gradually denser. Compared with the control sample, the connected porosity of AASR with the incorporation of 30%

and 50% RM increased for a given age, which is one of the main reasons for the reduction in compressive strength.

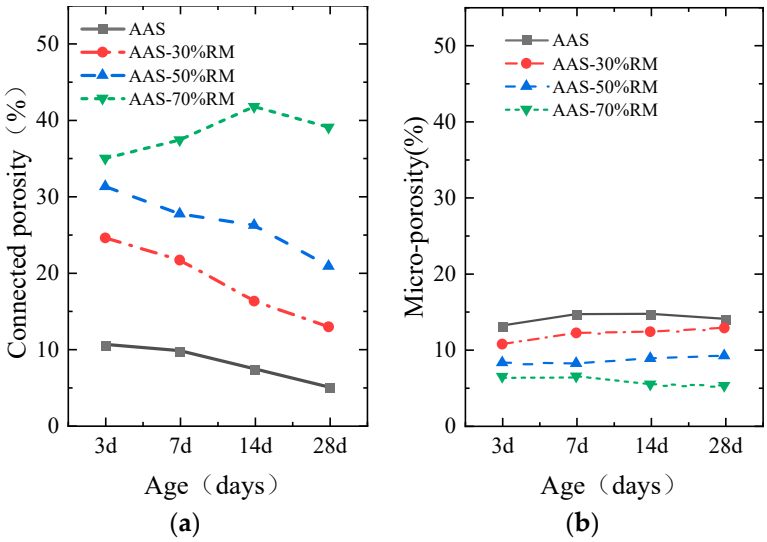


Figure 5. Connected porosity (**a**) and Micro-porosity (**b**) of AASR with different additions of RM.

Moreover, with the incorporation of 30% and 50% RM, the decrease rate of connected porosity becomes faster, indicating that the compactness of AASR is rapidly increased, which could be attributed to the high alkalinity provided by the RM. This agrees well with their development of compressive strength. As the content of RM reaches 70%, the connected porosity of AASR increased instead of decreasing, for 14 days, indicating that the densification process of this specimen is slower, which could be caused by the dilution effect of low active RM.

It has been shown that drying between 40 and 105 °C mainly reflects the bound water content in the microfine pores [21,22]. As can be seen from Figure 5b, unlike the development pattern of connected porosity, the micro-porosity of each specimen slightly increased with age, which is mainly due to the continuous formation of hydration products inside the specimen, resulting in the refinement of the pores, and, hence, increasing the proportion of micro-pores. Furthermore, as the RM content increased to 70%, the micro-porosity decreased the most, which indicates that the filling and refinement of the pores by the reaction products is smallest, and also indicating that the hydration reaction in this specimen is slowest.

Additionally, when compared with the control group of the same age, the micro-porosity of the sample decreases with the increase of RM admixture, while its connected porosity increases. This indicates that the addition of red mud introduces more harmful pores (50–200 nm) and multi harmful pores (>200 nm) in the specimen [23], which is detrimental to the mechanical properties of AASR [24].

3.2.2. Hydration Process

Figure 6 shows the heat evolution curves, as well as the cumulative heat release of hydration curves of AASRs samples. From Figure 6a, the hydration process can be divided into five distinctive regions: a rapid dissolution state, an induction state, an acceleration state, a deceleration state, and a stabilization state [25,26]. It has been shown that the first higher sharp exothermic peak that occurs after 0.2 h is usually the result of the rapid dissolution of the slag particles. After a very short induction period, the second exothermic peak appears, which is related to the formation of a coagulation structure from the hydration products C-A-S-H. It is worthy of note that with the increase of the RM content, the induction period is prolonged, and the peak of the acceleration period is decreased. Moreover, as the incorporation of RM is increased by up to 70%, the peak of

the acceleration period almost disappears, indicating that the silica-aluminous fraction in the red mud is difficult to leach, and the inert minerals such as hematite are less involved during the hydration reaction, thus generating less hydration products. This can also be supported by the results of accumulated exothermic heat from Figure 6b, which indicate that with the increase of RM content up to 70% RM the accumulated heat release decreased by about 54%.

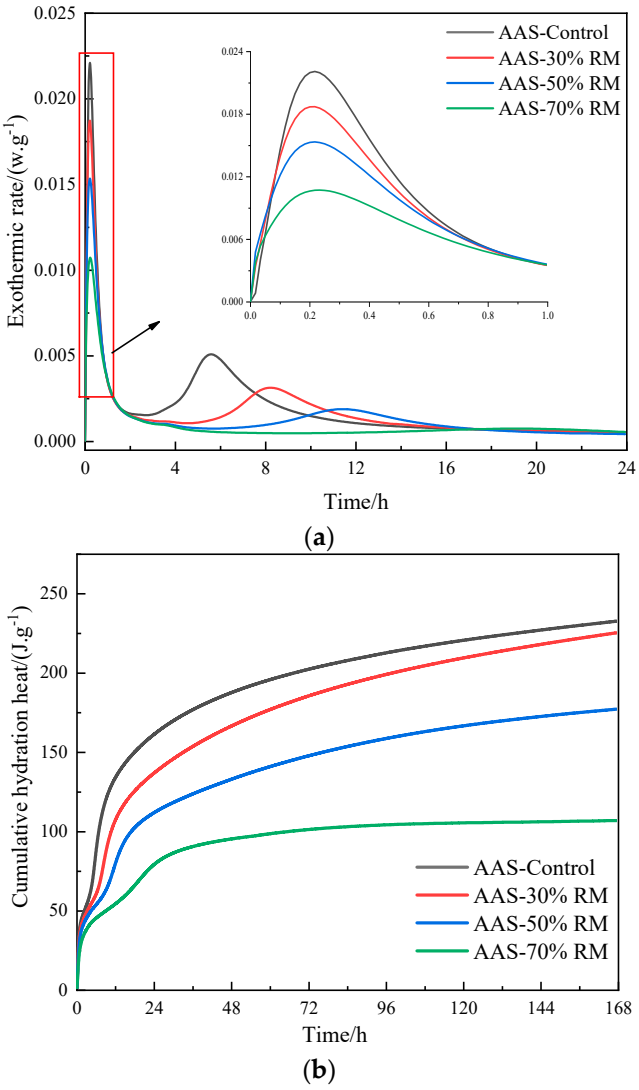


Figure 6. Exothermic rate curve of AASR (**a**) and cumulative hydration heat (**b**).

3.2.3. Phase Composition

1. XRD: The XRD patterns of all samples at 28 days are shown in Figure 7. It can be seen that the products of the control sample are mainly C-A-S-H gels with a disordered tholeite structure [10,27]. The main minerals of the AASR materials are hydrated calcium aluminosilicate ($CaAl_2Si_2O_8$-$4H_2O$), calcite ($CaCO_3$), hematite (Fe_2O_3), hard alumina monohydrate (AlO(OH)), and calcium chalcocite ($Al_6CCa_{0.4}H_{4.4}Na_{7.6}O_{29.2}Si_6$), which are consistent with the main mineral composition of the original red mud. Furthermore, as the content of RM increased, the intensity of diffraction peaks gradually became stronger, indicating that the red mud hardly participated in the alkali activated reaction, which corresponds well to the results from isothermal calorimetry.
2. FTIR: Due to the poor crystallinity of most of the AASR products, which was difficult to detect by the XRD, the FTIR test of each group of paste specimens were then carried out, and the results are shown in Figure 8. The absorption peaks, at around

3460 cm^{-1} and 1631 cm^{-1}, can be assigned to the stretching vibration of [O-H] from water molecules [28]. One important feature in Figure 8 is that the bending vibration absorption peaks and the stretching vibration absorption peaks, at around 982–1007 cm^{-1} and 466 cm^{-1}, which are assigned to the [Si-O] from C-A-S-H [29], became narrower with the increase of red mud content, indicating that the formation of the C-A-S-H gel is reduced. Moreover, bands at 1495 cm^{-1} and 872 cm^{-1} could be found in all specimens, which can be attributed to the anti-symmetric stretching and out-of-plane bending modes of CO_3^{2-} ions, indicating the presence of calcite (originated from raw material of red mud). After adding red mud, the intensity of these bands became stronger, and the more red mud that was introduced, the stronger the intensity of these bands. This indicates that the geopolymerization reaction is less as increase of red mud, which is in agreement with the XRD results.

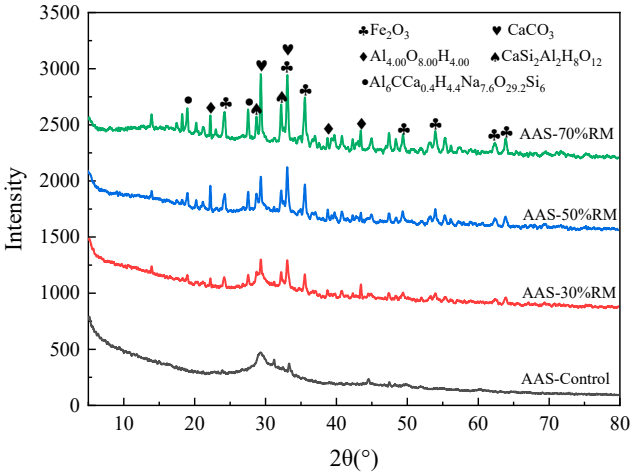


Figure 7. The XRD patterns of the alkali slag-red with different additions of RM.

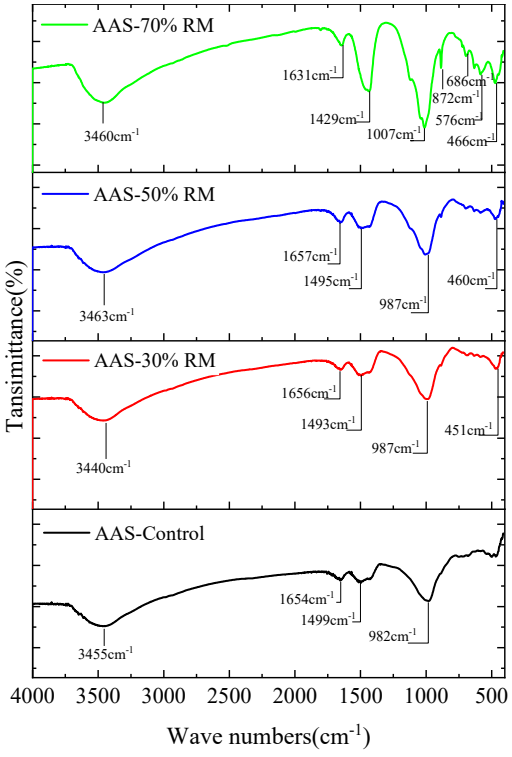


Figure 8. FTIR spectra of the AASR with different additions of RM.

3.2.4. Micromorphology Analysis

Figure 9 shows the 28-day results of BSE/EDS of AASR. It can be seen that the dissolution of silica-alumina precursors is not complete, and there are unhydrated slag and red mud particles in their hardened bodies. It can also be seen that with a proper content of red mud, the microstructure of AASR is denser, so a higher strength can be obtained. However, when the RM content increases to more than 50%, the microstructure becomes loose, and the degree of structural densification is reduced, leading to more cracks (Figure 10).

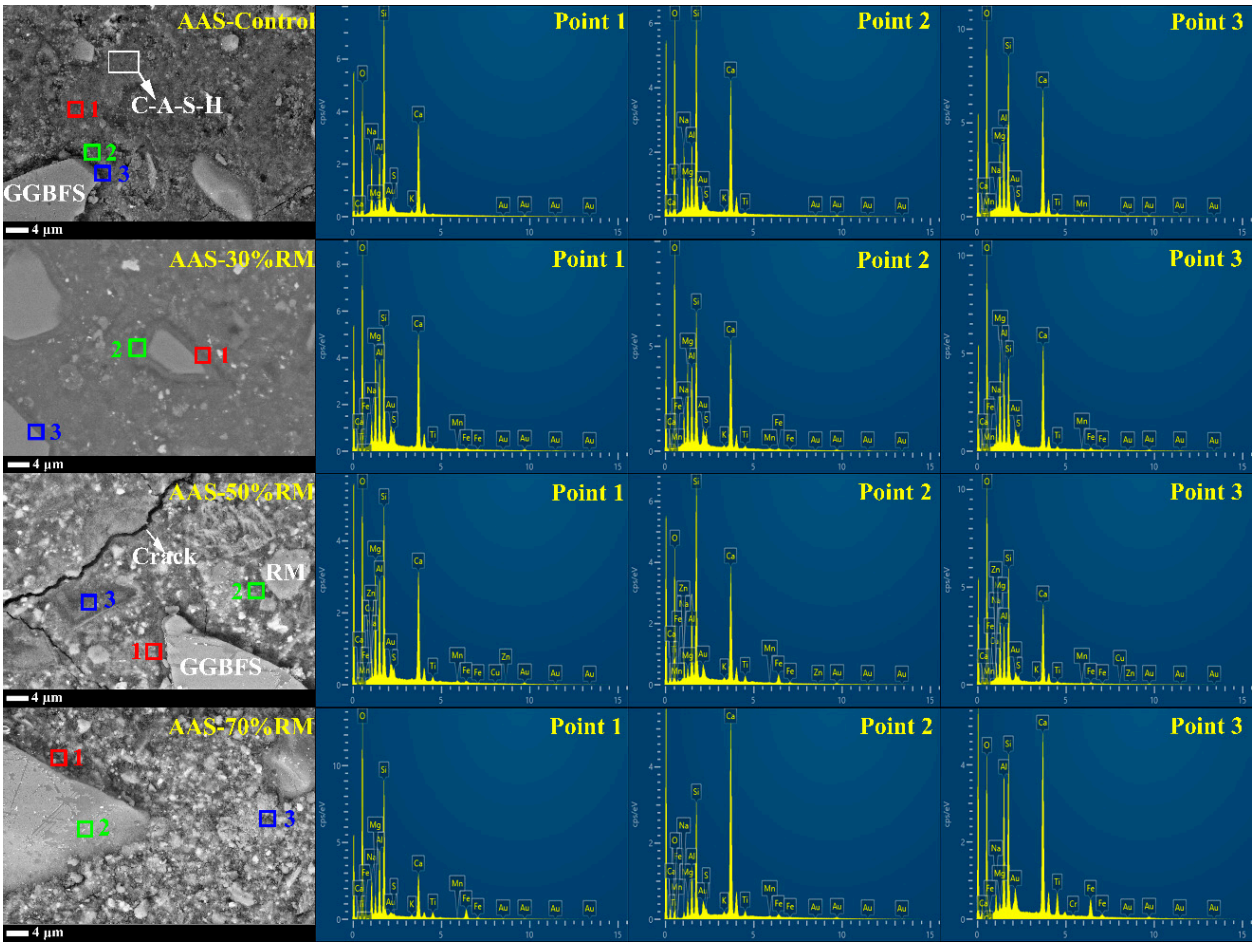


Figure 9. BSE/EDS images of alkali slag-red with different additions of RM.

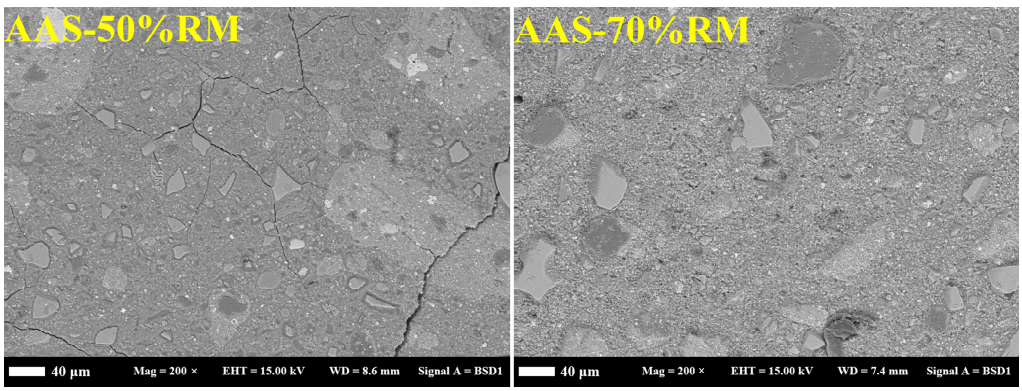


Figure 10. BSE images of alkali slag-red with different additions of RM.

Additionally, according to the surface scanning diagram in Figure 11, it is found that the distributions of Si, Ca, Na, and Mg elements are uniform, while Al elements show different degrees of enrichment, which is mainly caused by incomplete cleaning due to the embedding of polishing powder in surface pores during the process of polishing. Another important feature is that the distribution of Fe in the control group is small and uniform, while Fe elements show different degrees of enrichment and distribution in the C-A-S-H after adding red mud in AASR, which indicates that these hematites are difficult to dissolve into the hydration products.

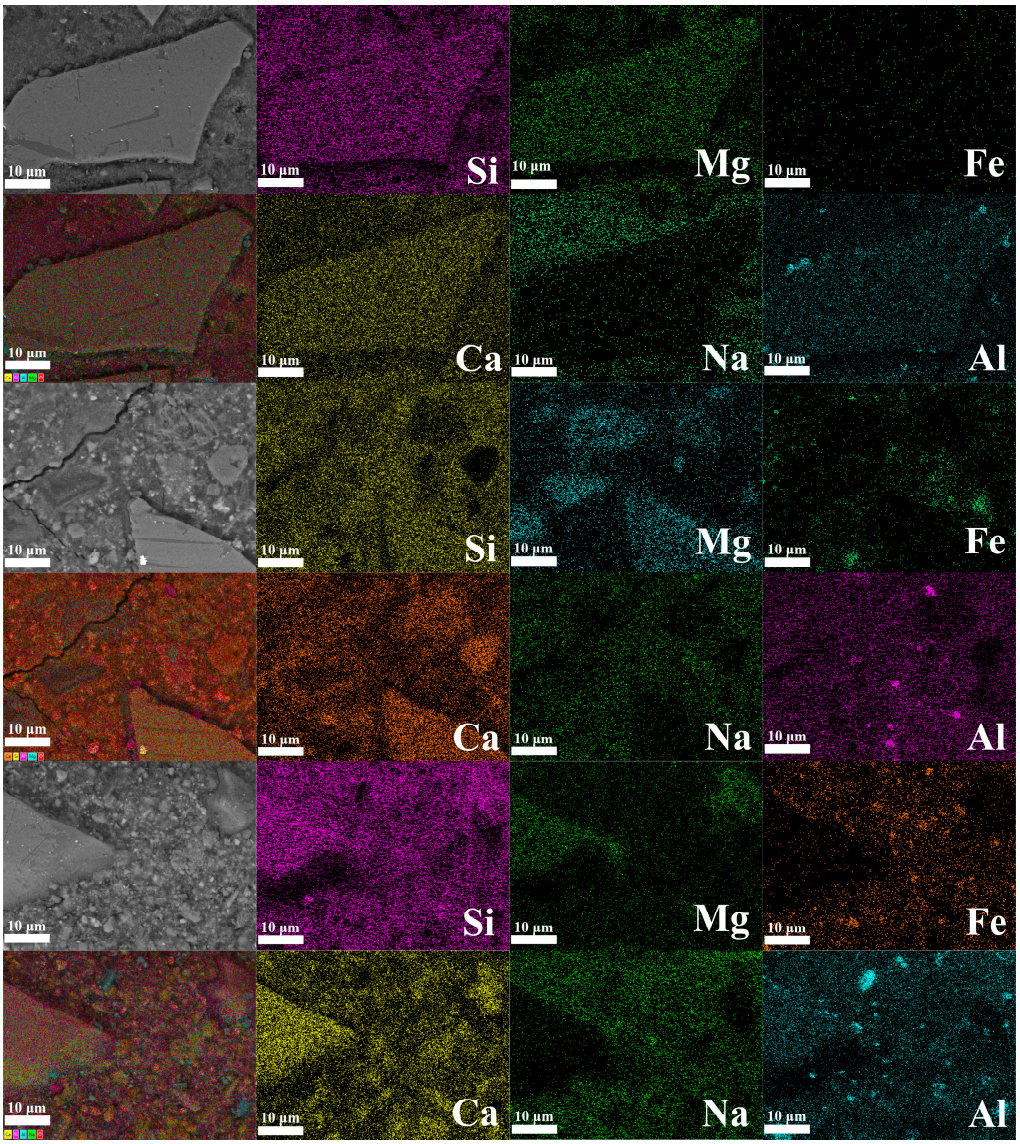


Figure 11. Elemental distribution of BSE-EDS surface sweep of RM with different additions.

Given the results of EDS, combined with the XRD analysis, it is plausible that the dissolved ionic species, including aluminates, calcium, silicates, and alkali ions, can form various types of amorphous phases, including calcium-silicate-hydrate (C-S-H), calcium-aluminosilicate-hydrate (C-A-S-H), and alkali aluminosilicate-hydrate (N-A-S-H), which provide the binding capabilities in AASR, so the decrease of compressive strength is more significant in the AASR blended with 70% red mud.

4. Conclusions

The conclusions on the law and mechanism of the effect of red mud admixture on the mechanical properties of AASR cementitious materials are as follows:

1. The addition of the proper amount of red mud makes the alkalinity of the AASR system increase, which is beneficial to the development of AASR strength, while when the amount of red mud is too great, the compressive strength at the same age decreases with the increase of red mud, and the 28-day compressive strength decreases by 78.8% compared with the baseline group.
2. The mechanism of the effect of red mud content on the compressive strength of AASR indicates that it is difficult to leach the silicon and aluminum components in red mud, as only a small part of red mud participates in hydration, the degree of hydration reaction of the system was low, and the formation of hydration products makes the strength of the system develop slowly.
3. Due to the difficulty of red mud dissolution, it slows down the hydration process of the AASR system, which makes the initial and final setting time longer.
4. The red mud content does not change the type of hydration products of the AASR cementitious material, but with the increase of red mud content, the amount of hydration generation decreases, which is one of the reasons for the reduction of the AASR system's compressive strength.
5. The addition of red mud introduces more harmful pores in the specimen, and when the content of red mud is 70%, the 28-day connected porosity reaches 39.05%; at the same time, the filling and refinement effect of the reaction products on the pores is small, resulting in a loose paste structure and reduced strength.

Author Contributions: Conceptualization, J.L.; data curation, J.L., K.Y., P.W. and L.Z.; writing—original draft preparation, J.L. and J.Y.; writing—review and editing, J.L., Q.L. and P.C.; supervision, P.C. and Q.L.; project administration, Q.L.; funding acquisition, P.C. and Y.M. All authors have read and agreed to the published version of the manuscript.

Funding: The authors acknowledge the following institutions for providing facilities and the financial support: National Natural Science Foundation of China (NO. 52268039); Guangxi Natural Science Foundation, China (NO. 2021GXNSFBA220047 and AD22035104); Open funds (NO. 22-J-21-21) from Guangxi key laboratory of new energy and building energy saving; and College student innovation project from Guilin University of Technology (NO. 202210596314).

Institutional Review Board Statement: Not applicable.

Informed Consent Statement: Not applicable.

Data Availability Statement: Not applicable.

Conflicts of Interest: The authors declare that they have no conflict of interest.

References

1. Gräfe, M.; Power, G.; Klauber, C. Bauxite residue issues: III. Alkalinity and associated Chemistry. *Hydrometallurgy* **2011**, *108*, 60–79. [CrossRef]
2. Occhicone, A.; Vukčević, M.; Bosković, I.; Mingione, S.; Ferone, C. Alkali-activated red mud and construction and demolition waste-based components: Characterization and environmental assessment. *Materials* **2022**, *15*, 1617. [CrossRef]
3. Oprčkal, P.; Mladenovič, A.; Zupančič, N.; Ščančar, J.; Milačič, R.; Serjun, V.Z. Remediation of contaminated soil by red mud and paper Ash. *J. Clean. Prod.* **2020**, *256*, 120440. [CrossRef]
4. Li, X.; Zhang, Q.; Mao, S. Investigation of the bond strength and microstructure of the interfacial transition zone between cement paste and aggregate modified by Bayer red Mud. *J. Hazard. Mater.* **2021**, *403*, 123482. [CrossRef]
5. Occhicone, A.; Vukčević, M.; Bosković, I.; Ferone, C. Red Mud-Blast Furnace Slag-Based Alkali-Activated Materials. *Sustainability* **2021**, *13*, 11298. [CrossRef]
6. Duxson, P.; Provis, J.L.; Lukey, G.C.; Van Deventer, J.S. The role of inorganic polymer technology in the development of 'green concrete'. *Cem. Concr. Res.* **2007**, *37*, 1590–1597. [CrossRef]
7. Zhang, J.; Li, S.; Li, Z.; Liu, C.; Gao, Y. Feasibility study of red mud for geopolymer preparation: Effect of particle size Fraction. *J. Mater. Cycles Waste Manag.* **2020**, *22*, 1328–1338. [CrossRef]

8. Li, Z.; Zhang, J.; Li, S.; Gao, Y.; Liu, C.; Qi, Y. Effect of different gypsums on the workability and mechanical properties of red Mud-slag based grouting Materials. *J. Clean. Prod.* **2020**, *245*, 118759. [CrossRef]
9. Chen, X.; Guo, Y.; Ding, S.; Zhang, H.; Xia, F.; Wang, J.; Zhou, M. Utilization of red mud in Geopolymer-based pervious concrete with function of adsorption of heavy metal Ions. *J. Clean. Prod.* **2019**, *207*, 789–800. [CrossRef]
10. Lemougna, P.N.; Wang, K.T.; Tang, Q.; Cui, X.M. Study on the development of inorganic polymers from red mud and slag system: Application in mortar and lightweight materials. *Constr. Build. Mater.* **2017**, *156*, 486–495. [CrossRef]
11. Zhang, P. *Optimized Design and Performance Study of Red Mud-Based Alkali-Inspired Cementitious Materials*; South China University of Technology: Guangzhou, China, 2016.
12. Garanayak, L. Strength effect of alkali activated red mud slag cement in ambient Condition. *Mater. Today Proc.* **2021**, *44*, 1437–1443. [CrossRef]
13. Liang, X.; Ji, Y. Preparation sequences and pretreatment optimization of Alkali-activated red mud and blast furnace slag-based Materials. *J. Mater. Cycles Waste Manag.* **2021**, *23*, 259–271. [CrossRef]
14. Gao, Y.; Li, Z.; Zhang, J.; Zhang, Q.; Wang, Y. Synergistic use of industrial solid wastes to prepare Belite-rich sulphoaluminate cement and its feasibility use in repairing Materials. *Constr. Build. Mater.* **2020**, *264*, 120201. [CrossRef]
15. Tian, K.; Wang, Y.; Dong, B.; Fang, G.; Xing, F. Engineering and Micro-properties of alkali-activated slag pastes with Bayer red Mud. *Constr. Build. Mater.* **2022**, *351*, 128869. [CrossRef]
16. *GB/T 17671-1999*; Method of Testing Cements-Determination of Strength. The State Bureau of Quality and Technical Supervision: Beijing, China, 1999; p. 9.
17. *ASTM C642*; Standard Test Method for Density, Absorption, and Voids in Hardened Concrete, Annual Book of ASTM Standards, 04.02. American Society for Testing and Materials: Philadelphia, PA, USA, 2002.
18. Romer, M. Effect of moisture and concrete composition on the Torrent permeability Measurement. *Mater. Struct.* **2005**, *38*, 541–547. [CrossRef]
19. Parrott, L.J. Moisture conditioning and transport properties of concrete test Specimens. *Mater. Struct.* **1994**, *27*, 460–468. [CrossRef]
20. Collins, F.G.; Sanjayan, J.G. Capillary Shape: Influence on Water Transport within Unsaturated Alkali Activated Slag Concrete. *J. Mater. Civ. Eng.* **2010**, *22*, 260–266. [CrossRef]
21. Li, Q.; Li, X.; Yang, K.; Zhu, X.; Gevaudan, J.P.; Yang, C.; Basheer, M. The Long-term failure mechanisms of alkali-activated slag mortar exposed to wet-dry cycles of sodium Sulphate. *Cem. Concr. Compos.* **2021**, *116*, 103893. [CrossRef]
22. Li, Q.; Yang, Y.; Yang, K.; Chao, Z.; Tang, D.; Tian, Y.; Wu, F.; Basheer, M.; Yang, C. The role of calcium stearate on regulating activation to form stable, uniform and flawless reaction products in alkali-activated slag Cement. *Cem. Concr. Compos.* **2019**, *103*, 242–251. [CrossRef]
23. Wang, H. *Research and Application of High Performance Water Glass Suspension Type Double Liquid Grouting Material*; Wuhan University of Technology: Wuhan, China, 2007.
24. Wu, Z. Green high performance concrete—The direction of concrete development. *China Concr. Cem. Prod.* **1998**, *1*, 3–6.
25. Pacewska, B.; Wilińska, I. Usage of supplementary cementitious materials: Advantages and limitations: Part I. C–S–H, C–A–S–H and other products formed in different binding Mixtures. *J. Therm. Anal. Calorim.* **2020**, *142*, 371–393. [CrossRef]
26. Zhang, J.; Li, G.; Ye, W.; Chang, Y.; Liu, Q.; Song, Z. Effects of ordinary Portland cement on the early properties and hydration of calcium sulfoaluminate Cement. *Constr. Build. Mater.* **2018**, *186*, 1144–1153. [CrossRef]
27. Qaidi, S.M.; Tayeh, B.A.; Isleem, H.F.; de Azevedo, A.R.; Ahmed, H.U.; Emad, W. Sustainable utilization of red mud waste (bauxite residue) and slag for the production of geopolymer composites: A Review. *Case Stud. Constr. Mater.* **2022**, *16*, e00994. [CrossRef]
28. Lu, B.; Shi, C.; Zhang, J.; Wang, J. Effects of carbonated hardened cement paste powder on hydration and microstructure of Portland Cement. *Constr. Build. Mater.* **2018**, *186*, 699–708. [CrossRef]
29. Bayat, A.; Hassani, A.; Yousefi, A.A. Effects of red mud on the properties of fresh and hardened Alkali-activated slag paste and Mortar. *Constr. Build. Mater.* **2018**, *167*, 775–790. [CrossRef]

Disclaimer/Publisher's Note: The statements, opinions and data contained in all publications are solely those of the individual author(s) and contributor(s) and not of MDPI and/or the editor(s). MDPI and/or the editor(s) disclaim responsibility for any injury to people or property resulting from any ideas, methods, instructions or products referred to in the content.